PHYSICAL REVIEW B VOLUME 57, NUMBER 12 15 MARCH 1998-II

Mechanism of the low-ejection-energy $(e,2e)$ reaction on a graphite surface

A. S. Kheifets*
Dipartimento di Fisica, Università di Roma Tre, Via della Vasca Navale 84, 00146 Roma, Italy

S. Iacobucci
Istituto Metodologie Avanzate Inorganiche del CNR, CP10, I-00016 Monterotondo Scalo, Italy

A. Ruocco
Dipartimento di Fisica, Università di Roma Tre, Via della Vasca Navale 84, 00146 Roma, Italy

R. Camilloni
Istituto Metodologie Avanzate Inorganiche del CNR, CP10, I-00016 Monterotondo Scalo, Italy

G. Stefani
Dipartimento di Fisica, Università di Roma Tre, Via della Vasca Navale 84, 00146 Roma, Italy

(Received 29 October 1997)

We develop a theoretical model to describe a slow electron ejection from a crystal by electron impact at a moderate incident energy. The electron impact ionization is considered within the first Born approximation. The projectile is treated as a plane wave whereas the target electron initial and final states are described by the bulk one-electron wave functions in the momentum space representation. To allow the ionized electron to escape from the crystal the final state in the bulk of the crystal is matched in energy and a parallel component of momentum by a plane wave in the vacuum. This theoretical model is used to simulate the binding-energy spectra obtained by the grazing-angle reflection mode $(e,2e)$ reaction on the surface of highly oriented pyrolytic graphite. [S0163-1829(98)03011-2]

I. INTRODUCTION

Electron momentum spectroscopy based on the $(e,2e)$ reaction has been introduced recently as a technique to study the electronic structure of solids.[1,2] In the $(e,2e)$ reaction an incident electron knocks out a target electron, with subsequent detection of both outgoing electrons in time coincidence with fully determined kinematics. This allows us to infer the binding energy and momentum of the target electron *before* the collision by using the laws of energy and momentum conservation.

At present, the $(e,2e)$ reaction on solid targets is performed in two different modes. In the transmission $(e,2e)$ experiments the incident electron is impinged on an ultrathin target membrane and the two outgoing electrons emerge from the side of the target opposite to the electron gun. In the reflection $(e,2e)$ reaction both the electron gun and the two electron detectors are placed at the same side of the target.

The transmission mode $(e,2e)$ experiments are performed under conditions of a high incident energy and a large momentum transfer. This allows us to interpret an $(e,2e)$ event as a free-electron-like binary collision between the projectile and the target electron. The cross section of such a binary $(e,2e)$ reaction is directly proportional to the number of target electrons in the given range of binding energy and momentum. This transparent physical interpretation of the high-energy transmission mode $(e,2e)$ makes it very attractive for studying the electronic structure of solids. However, its practical implementation is hampered by laborious and painstaking fabrication of ultrathin free-standing membranes.

To avoid this difficulty there have been experiments successful in using diffracted electron beams in reflection from a solid surface. Two different experimental geometries have been used. Kirschner, Artamonov, and Samarin[3] reported backscattering reflected mode $(e,2e)$ on the surface of tungsten. Because they employed the time-of-flight detection technique the incident energy was very low (14–25 eV). Interpretation of this low energy $(e,2e)$ required quite an elaborate theory that employed LEED-type wave functions both for the incident and the two outgoing electrons.[4] The calculated cross section contained the target electron wave function in the valence band which, however, could not be easily factored out. So the information about the occupied target states could not be extracted directly from the measured $(e,2e)$ cross section.

Another type of reflection mode $(e,2e)$ experiment was performed by Iacobucci *et al.*[5,6] on the surface of highly oriented pyrolytic graphite (HOPG). They used a moderate incident energy of 300 eV in a grazing-angle reflection geometry. An attempt has been made to use this type of $(e,2e)$ reaction to map energy bands of graphite.[7] The peak positions in the measured binding energy spectra were consistent with theoretical band energies. The peak intensities were also analyzed and at least for the topmost π band were found to agree rather well with the theoretical density of states.

This gives an indication that the grazing angle $(e,2e)$ at moderate incident energies can be used to extract electronic structure information about the target. Still, a consistent theory is required to deal with the scattering dynamics and the ionization mechanism. This theory is outlined in the present paper. Conceptually, it is similar to the three-step model of volume photoionization from solids.[8] We assume that the ionizing collision takes place in the bulk of the solid. Then the ionized electron propagates to the surface and escapes to the vacuum. The assumption of the volume ionization is particularly justified for graphite, which, as a layered material, retains much of its electronic structure up to the topmost surface layer.

We describe the ionizing collision in the first Born approximation, i.e., we assume that the projectile interacts with the target electron only once. Thus we neglect multiple scattering processes, both elastic and inelastic. We also assume, in accordance with Iacobucci *et al.*,[5] that the ionizing collision is caused by the projectile that is specularly reflected from the target. Berakdar and Das[9] explored other mechanisms of the reflection mode $(e,2e)$ in which one or both of the outgoing electrons are reflected. However, for the present grazing-angle geometry, the ionization caused by the specularly reflected incident electron is strongly dominant since it is kinematically possible with the smallest amount of the momentum transfer. Thus the Born ionization amplitude, which is inversely proportional to the squared momentum transfer, is largest. Interestingly enough, Artamonov, Samarin, and Kirschner[10] have demonstrated that the same is true for the reflection mode $(e,2e)$ in the backscattering geometry. Their measured $(e,2e)$ intensity showed clear symmetry with respect to the direction of the specularly reflected incident beam.

To calculate the Born ionization amplitude we employ the bulk target electron wave functions in the momentum space representation. We use the extended zone scheme in which every momentum space wave function has a dominating presence in only one particular Brillouin zone. In the momentum space representation the Born transition amplitude is equal to the product of the wave functions of the initial state in the occupied valence band and the final empty state in the conduction band. In the limit of high-energy transfer the final state becomes a plane wave and has the momentum space wave function equal to unity. Thus we arrive at the usual high-energy $(e,2e)$ formalism in which the measured $(e,2e)$ intensity is proportional to the squared momentum space wave function of the occupied target state.

To allow the ejected electron to escape from the crystal to the vacuum we require that the energy and the parallel component of the momentum in the bulk should be matched by those of a plane wave in the vacuum. In a three-dimensional (3D) crystal with a strong dispersion of the energy bands with respect to the perpendicular component of the momentum this can be achieved by adjusting this component, which is not bound by the law of momentum conservation. In graphite, because of its quasi-2D structure, the band energy in the valence band and low conduction band depends very weakly on the perpendicular component of the momentum. This makes the matching very restrictive, especially at a small ejected electron energy. However, as the energy of the ejected electron increases its wave function gradually acquires the 3D character and the matching is easily achieved.

At a small momentum transfer the electron impact causes nearly vertical transitions in the target momentum space. This projects the kinematically determined ejected electron state in the vacuum onto a well-defined compact region in the valence electron momentum space. However, this direct mapping of the valence band can be modified by a surface reciprocal lattice vector acquired when the ejected electron propagates through the crystal. The kinematics of the grazing-angle reflection mode $(e,2e)$ experiments on graphite[5,6] is such that the vertical transitions at a small ejection energy originate in the first Brillouin zone where only two bands σ_1 and π have significant presence. However, if the momentum balance is modified by a surface reciprocal lattice vector the same ejected electron state can originate from the second or third Brillouin zones where the other σ_2 and σ_3 bands are populated. This explains why the binding energy spectra of graphite observed by the grazing-angle reflection mode $(e,2e)$ reaction contain the signature of all four valence bands.[7]

The rest of the paper is organized according to the following plan. In Sec. II we present the momentum density formalism and apply it to describe various types of ionization processes (electron impact ionization and photoionization) in the bulk of a solid. In Sec. III we present our numerical results for the reflection $(e,2e)$ reaction on the surface of highly oriented pyrolytic graphite (HOPG) and compare our calculation with the experimental data of Iacobucci *et al.*[5,6] Conclusions and possible extension of the present theory are made in Sec. IV.

II. MOMENTUM SPACE WAVE-FUNCTION FORMALISM

In a crystal the electron wave function can be written as the sum of the Bloch waves:

$$\psi_{j\mathbf{k}}(\mathbf{r})=\Omega^{-1/2}\sum_{\mathbf{G}} C_j(\mathbf{k}+\mathbf{G})e^{i(\mathbf{k}+\mathbf{G})\cdot\mathbf{r}}, \tag{1}$$

where $\mathbf{k}$ is the crystal momentum, $\mathbf{G}$ the reciprocal lattice vector. The band index j labels different bands with generally different energies $E_{j\mathbf{k}}$. The wave function (1) is normalized in the unit cell of the volume Ω. The coefficients $C_j(\mathbf{k}+\mathbf{G})$ give the momentum space representation of the wave function $\psi_{j\mathbf{k}}$:[11]

$$\psi_{j\mathbf{k}}(\mathbf{q})=(2\pi)^{-3/2}\int_{\Omega} e^{-i\mathbf{qr}}\psi_{j\mathbf{k}}(\mathbf{r})d\mathbf{r}$$

$$=\sqrt{\frac{\Omega}{(2\pi)^3}}\sum_{\mathbf{G}} C_j(\mathbf{k}+\mathbf{G})\,\delta_{\mathbf{k}+\mathbf{G},\mathbf{q}}. \tag{2}$$

The periodicity in the reciprocal space makes it sufficient to define the crystal momentum $\mathbf{k}$ within the first Brillouin zone (first BZ). However, the completeness of the Fourier transformation (2) requires $\mathbf{q}$ to be defined in the whole momentum space. To ensure the orthonormality of the wave function (1) the momentum space coefficients should satisfy the following sum rule:

$$\sum_{\mathbf{G}} C_j(\mathbf{k}+\mathbf{G})C^*_{j'}(\mathbf{k}'+\mathbf{G})=\delta_{\mathbf{kk}'}\delta_{jj'}. \tag{3}$$

We note the following property of the momentum space coefficients $C_j(\mathbf{q})$. The lowest (in energy) band has the largest value of $|C_j(\mathbf{q})|$ at $\mathbf{q}\in$ first BZ. The second-lowest band

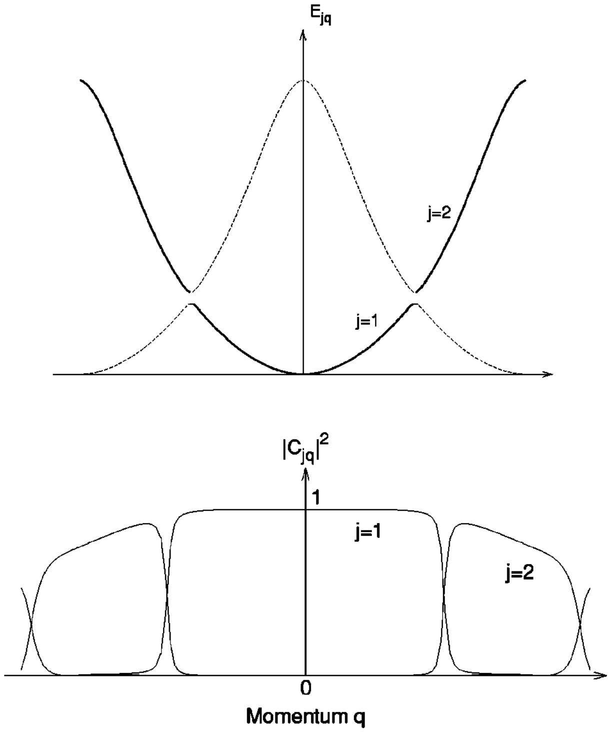

FIG. 1. Top: unfolding of the free-electron parabola into repeated energy bands. Bottom: free-electron momentum density.

has the largest presence at $\mathbf{q}\in$ second BZ, etc. Although we do not produce a rigorous proof of this statement, we illustrate it in the case of a weak periodic potential imposed on a free-electron gas. In this case the one-electron energy plotted in the extended zone scheme follows a free-electron parabola except for the discontinuity near the BZ boundaries. The one-electron wave functions are plane waves and have therefore only one momentum space coefficient $C_j(\mathbf{k}+\mathbf{G})$ approximately equal to unity with exception of the values near the BZ boundaries where reflection from the periodic potential becomes significant. In the repeated zone scheme each section of the parabola corresponding to a given BZ unfolds into a separate energy band as shown in Fig. 1. Each band j can be assigned with the momentum space coefficient $C_j(\mathbf{q})$ formally defined for $\mathbf{q}$ in the whole momentum space. However, it is obvious from the way we extended the one-electron parabola into repeating bands that $C_j(\mathbf{q})$ is only significant in one particular BZ whereas it is nearly zero in all other sections of the extended momentum space as illustrated in Fig. 1.

In a real crystal this selective population of the momentum space by various bands will depend very much on how well this crystal can be described by a free-electron model. In a complex solid with more than two spin-degenerate valence electrons per unit cell the band index should also absorb the one-electron quantum numbers that distinguish inequivalent electrons. So there might be more than one band occupied in the given section of the BZ. In the case of graphite, the one-electron quantum numbers indicate the symmetry with respect to the reflection in the basal plane. Accordingly, the energy bands in graphite are classified as σ and π.

The selectivity of the momentum space wave functions in graphite is illustrated in Fig. 2 in which we plot the energy bands and the band resolved momentum densities,

$$\rho_j(\mathbf{q}) = \Omega(2\pi)^{-3}\left|\sum_{\mathbf{G}} C_j(\mathbf{k}+\mathbf{G})\,\delta_{\mathbf{q},\mathbf{k}+\mathbf{G}}\right|^2, \tag{4}$$

along the HCP symmetry lines. For the two basal plane directions ΓK and ΓM only various σ bands contribute to the electron momentum density. In the first BZ the lowest σ_1 band is most intense whereas in the second and third BZ the population switches to the higher σ_2 and σ_3 bands (see Fig. 3). The π band has no contribution to the momentum density in the basal plane. This is so because the symmetry of the π orbitals requires the Fourier integral (2) to reverse its sign when the $\mathbf{q}$ vector is reflected with respect to the basal plane. Obviously this reflection does not change $\mathbf{q}$ for the in-plane

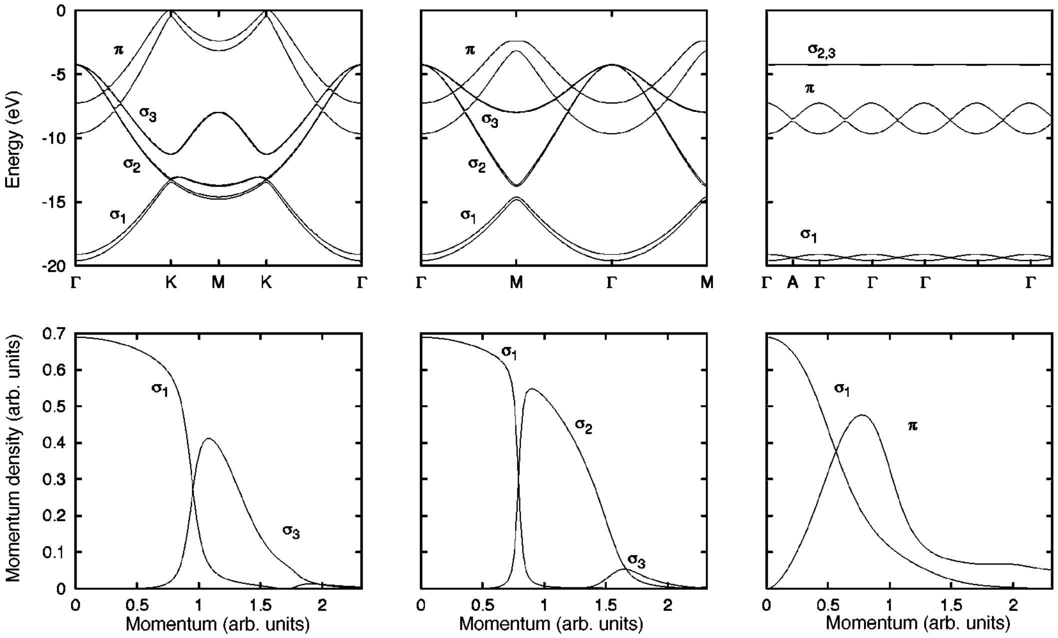

FIG. 2. Band energies (top panel) and momentum densities (bottom panel) in graphite along three symmetry lines ΓK, ΓM, and ΓA.

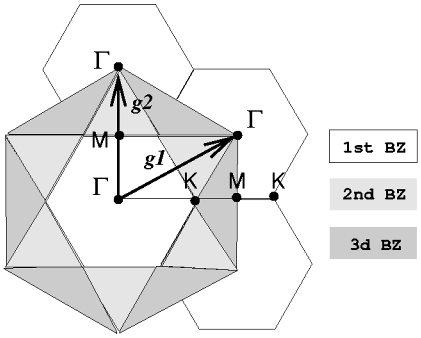

FIG. 3. Basal plane projections of different Brillouin zones in graphite. Different BZ are shown in different shades of gray. The shortest reciprocal vectors of the surface are indicated as $\mathbf{g}_1$ and $\mathbf{g}_2$.

directions. Hence the π momentum density is zero. The π band has nonzero intensity for the out-of-plane ΓA direction. This direction is somewhat abnormal since it corresponds to the electron motion between the distant and weakly bonded sheets of carbon atoms. Hence the electron energy shows very little dispersion and only the lowest σ_1 band is populated.

Let us now apply the formalism of the momentum space wave functions to the ionization process. We consider a fast electron inelastic collision with the bulk of a solid, which results in the ejection of a slow ionized electron into the vacuum. We adopt the following notations. We label the incident, the fast (scattered), and the slow (ejected) electrons by the indices $i=0$, 1, and 2, respectively. The electron momenta and the energies in the vacuum are correspondingly $\mathbf{p}_i$ and E_i. The fast electrons (incitent and scattered) are represented by the plane waves $|\mathbf{p}_i\rangle=(2\pi)^{-3/2}\exp(i\mathbf{p}_i\mathbf{r})$, $i=0,1$. Hereafter we use the atomic units in which $\hbar=e=m=1$ and the unit of momentum is $a_0^{-1}=1.89$ Å^{-1}.

The electron momenta in the bulk are modified by the refraction on the crystal surface:

$$\mathbf{q}_{i\|}=\mathbf{p}_{i\|},$$

$$\mathbf{q}_{i\perp}=\sqrt{\mathbf{p}_{i\perp}^2+2V}. \tag{5}$$

Here V is the inner crystal potential acting upon the electron. When interpreting the photoemission experiments on simple metals this potential is usually set to the sum of the muffin-tin zero potential V_0 and the work function Φ.[8] By doing so one assumes that the unoccupied (conduction) and occupied (valence) energy bands can be derived from the same free-electron-like parabola in extended momentum space. The conduction band of graphite is derived from different one-electron states and unfolds into separate π and σ^* parabolas. The bottom of these parabolas is closer to the Fermi level rather than the muffin-tin zero (see Fig. 6 and corresponding discussion in Sec. III). Therefore we set here $V=\Phi$.

The target electron states before and after the collision are denoted as $|j\mathbf{k}\rangle$ and $|j_2\mathbf{k}_2\rangle$ and represented by the bulk wave functions (1). The slow ejected electron energy and the parallel component of the momentum are required to match those of a plane wave in the vacuum:

$$\mathbf{q}_{2\|}=\mathbf{p}_{2\|}-\mathbf{g},$$

$$E_{j_2\mathbf{k}_2}=E_2+\Phi. \tag{6}$$

Here $\mathbf{g}$ is a 2D reciprocal lattice vector parallel to the crystal surface.

The fully resolved cross section of the electron impact ionization can be presented in the form[13]

$$\frac{d\sigma}{d^3\mathbf{p}_1 d^3\mathbf{p}_2}=\frac{(2\pi)^4 N}{p_0}\sum_{jj_2} \times\int\int d^3\mathbf{k}d^3\mathbf{k}_2|\langle\mathbf{q}_1 j_2\mathbf{k}_2|U|j\mathbf{k}\mathbf{q}_0\rangle|^2 \times\delta(E_0-E_1-E_{j_2\mathbf{k}_2}+E_{j\mathbf{k}})\,\delta(E_2+\Phi-E_{j_2\mathbf{k}_2}) \times\delta(\mathbf{p}_{2\|}-\mathbf{q}_{2\|}-\mathbf{g}). \tag{7}$$

Since the target wave functions are normalized to the unit cell Eq. (7) contains the number of the unit cells in the target N. The matrix element of the Coulomb interaction between the plane-wave projectile and the target electron can be reduced to the Born transition amplitude:

$$\langle\mathbf{q}_1 j_2\mathbf{k}_2|U|j\mathbf{k}\mathbf{q}_0\rangle=\frac{\langle j_2\mathbf{k}_2|e^{-i\mathbf{Qr}}|j\mathbf{k}\rangle}{2\pi^2Q^2\epsilon(Q,\omega)}, \tag{8}$$

where $\mathbf{Q}=\mathbf{q}_0-\mathbf{q}_1$ and $\omega=E_0-E_1$ are the momentum and energy transfer from the projectile to the target electron. The dielectric function $\epsilon(Q,\omega)$ describes the screening of the pair Coulomb interaction between the projectile and the target electron by the rest of the many-electron ensemble. In Eq. (8) we neglect the exchange between the fast scattered electron and the excited target electron.

The Born transition amplitude between the target states in Eq. (8) is easily calculated using the momentum space representation (1):

$$\langle j_2\mathbf{k}_2|e^{-i\mathbf{Qr}}|j\mathbf{k}\rangle=\sum_{\mathbf{G},\mathbf{G}_2}C_{j2}^*(\mathbf{k}2+\mathbf{G}_2)C_j(\mathbf{k}+\mathbf{G}) \times\delta_{\mathbf{k}+\mathbf{G}+\mathbf{Q},\mathbf{k}_2+\mathbf{G}_2}. \tag{9}$$

Upon substituting Eqs. (8) and (9) into Eq. (7) we obtain the following expression:

$$\frac{d\sigma}{d^3\mathbf{p}_1 d^3\mathbf{p}_2}=\frac{(2\pi)^4}{p_0}\frac{f_{ee}N}{\epsilon(Q,\omega)}\sum_{jj_2}\int\int d^3\mathbf{k}d^3\mathbf{k}_2\left|\sum_{\mathbf{G},\mathbf{G}_2}C_{j2}^*(\mathbf{k}2+\mathbf{G}_2)C_j(\mathbf{k}+\mathbf{G})\,\delta_{\mathbf{k}+\mathbf{G}+\mathbf{Q},\mathbf{k}_2+\mathbf{G}_2}\right|^2\delta(E_0-E_1-E_{j_2\mathbf{k}_2}+E_{j\mathbf{k}})\,\delta(E_2+\Phi-E_{j_2\mathbf{k}_2})\,\delta(\mathbf{p}_{2\|}-\mathbf{q}_{2\|}+\mathbf{g}). \tag{10}$$

Here $f_{ee}=(2\pi^2Q^2)^{-2}$ is the Mott cross section of the electron-electron scattering in which we neglect exchange between the slow ejected and fast scattered electrons. The integration over $\mathbf{k}_2$ and the summation over $\mathbf{G}_2$ is eliminated by the δ functions, which ensure the matching condition of Eq. (6). Finally we arrive at the following expression:

$$\frac{d\sigma}{d\Omega_1 d\Omega_2 dE_1 dE_2} = (2\pi)^4 \frac{p_1 p_2}{p_0} \frac{f_{ee} N}{\epsilon(Q,\omega)} \times \int d^3\mathbf{k} \sum_{jj_2\mathbf{g}} \left| \sum_{\mathbf{G}} C^*_{j_2}(\mathbf{p}_{2\parallel} - \mathbf{g}, q_{2\perp}) \times C_j(\mathbf{k}+\mathbf{G})\, \delta_{\mathbf{k}+\mathbf{G}+\mathbf{Q},\mathbf{q}_2} \right|^2 \times \delta(E_0 - E_1 - E_2 + E_{j\mathbf{k}} - \Phi). \tag{11}$$

Here the perpendicular momentum component of the target electron $q_{2\perp}$ is fixed by the energy conservation (6). By introducing the spectral momentum density (SMD) of the target electrons

$$\rho(\mathbf{q},\varepsilon) = \sum_j \int d^3\mathbf{k} \sum_{\mathbf{G}} |C_j(\mathbf{k}+\mathbf{G})|^2 \delta_{\mathbf{k}+\mathbf{G},\mathbf{q}} \delta(\varepsilon - E_{j\mathbf{k}}), \tag{12}$$

Eq. (11) can be rewritten in the compact form

$$\frac{d\sigma}{d\Omega_1 d\Omega_2 dE_1 dE_2} = (2\pi)^4 \frac{p_1 p_2}{p_0} \frac{f_{ee} N}{\epsilon(Q,\omega)} \times \sum_{j_2\mathbf{g}} |C_{j_2}(\mathbf{q}_2)|^2 \rho(\mathbf{q},\varepsilon)\, \delta_{\mathbf{q}+\mathbf{Q},\mathbf{q}_2}, \tag{13}$$

where $\mathbf{q} = \mathbf{q}_1 + \mathbf{q}_2 - \mathbf{q}_0$ and $\varepsilon = E_1 + E_2 - E_0 + \Phi$.

In the regime of a high-energy (e,2e) Eq. (13) can be further simplified. We can neglect refraction and set $\mathbf{q}_i = \mathbf{p}_i$. The momentum space coefficient $C_{j_2}(\mathbf{q}_2)$ becomes unity for the single band j_2, which corresponds to the section of the one-electron parabola with the given momentum $\mathbf{q}_2$ (see Fig. 1). In the binary regime one can neglect the response of the other electrons in the solid and discard the dielectric function. Thus we finally arrive at the expression that is traditionally used to analyze the high-energy (e,2e) reaction:[1]

$$\frac{d\sigma}{d\Omega_1 d\Omega_2 dE_1 dE_2} = (2\pi)^4 \frac{p_1 p_2}{p_0} f_{ee} N \rho(\mathbf{q},\varepsilon). \tag{14}$$

Comparing Eq. (13) and Eq. (14) we see that the low-energy (e,2e) cross section contains the momentum space wave function in the final state above the vacuum level and hence can be used to study unoccupied states in solids. In this respect it is complementary to the high-energy (e,2e) reaction, which probes the valence states only.

III. NUMERICAL RESULTS

We apply the momentum space formalism derived in the previous section to simulate the experimentally observed binding-energy spectra from the surface of HOPG.[5–7] These spectra were obtained by the grazing-angle reflection mode (e,2e) reaction with the following kinematical parameters. The scattered electron energy E_1 were maintained constant at 300 eV while the incident energy E_0 was adjusted to span the range of binding energies of the valence band of graphite (approximately 20 eV). There were three sets of measurements taken at the ejected electron energies $E_2 =$ 3.7, 8.0, and 14.2 eV. The incident and scattered electrons were in the same plane with the azimuthal angles $\theta_0 = \theta_1 = 6°$. The slow ejected electrons were collected within a cone formed by the azimuthal angle $\theta_2 = 42.3 \pm 3°$ and the polar angle $\phi_2 = 2\pi$. This kinematical arrangement is illustrated in Fig. 4.

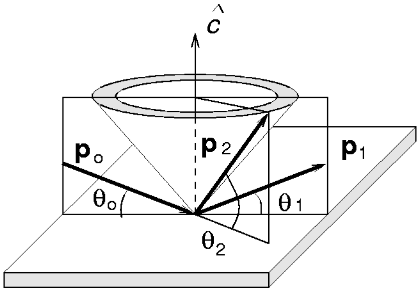

FIG. 4. Geometry of a grazing-angle reflection (e,2e) experiment. Arrows indicate incident $\mathbf{p}_0$, scattered $\mathbf{p}_1$, and ejected $\mathbf{p}_2$ electrons. The shaded area shows the acceptance range of the ejected electron momenta.

Of the various dynamical models suggested for the reflection mode (e,2e) by Berakdar and Das[9] we accept the mechanism suggested by Iacobucci *et al.*[5] as the dominating one. In this mechanism the projectile reflects specularly from the target and then scatters inelastically from the bound electron as illustrated in Fig. 5. This mechanism is strongly dominant because it is kinematically possible with the smallest amount of momentum transfer $Q = p_0 - p_1 \simeq \epsilon/\sqrt{2E_0} \ll 1$. Other mechanisms in which the (e,2e) event is caused directly by the incident electron have much larger momentum transfer $Q = 2p_0 \sin\theta_0 \sim 1$. They are strongly suppressed by the dynamical factor f_{ee} of Eq. (13), which is proportional to Q^{-4}. The conjugant process, in which the inelastic scattering takes place first and then the two outgoing electrons are reflected specularly from the crystal, is not considered separately here since it is described by the same formulas as the main mechanism within the present theory.

The binding-energy spectra obtained from the experiment can be simulated by the following theoretical expression:

$$I(\varepsilon) = \int_{\Delta\Omega_2} \frac{d\sigma}{d\Omega_1 d\Omega_2 dE_1 dE_2} d\Omega_2 \propto f_{ee} \int_{\Delta\Omega_2} d\Omega_2 \sum_{j_2\mathbf{g}} |Cj_2(\mathbf{p}_{2\parallel} - \mathbf{g}, q_{2\perp})|^2 \rho(\mathbf{q},\varepsilon)\, \delta_{\mathbf{q}+\mathbf{Q},\mathbf{q}_2}. \tag{15}$$

Here the solid angle integration is performed over the acceptance angle of the slow ejected electron detector. We omitted

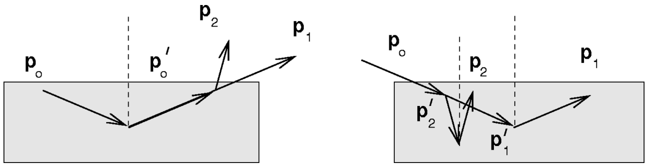

FIG. 5. Left: Dominant mechanism of the grazing-angle reflection mode (e,2e) reaction. Specular reflection is followed by inelastic scattering. Right: Conjugate process in which inelastic scattering is followed by specular reflection.

TABLE I. Boundaries of the valence electron momentum probed by the grazing-angle $(e,2e)$ reaction with the assumption of the direct escape of the ionized electrom into the vacuum.

Ejected electron energy E_e (eV)	Target electron momentum (a.u.) $q_\parallel^{\min}$	$q_\parallel^{\max}$	$q_\perp^{\min}$	$q_\perp^{\max}$
3.7	0.35	0.57	0.67	0.68
8.0	0.35	0.67	0.83	0.86
14.2	0.47	0.90	0.95	1.00

the dielectric function from Eq. (13) and thus neglected the screening of the Coulomb potential, which is a justified assumption for such a poor metal as graphite.[14] However, by discarding the dielectric function we also neglected the collective excitations which can strongly modify the binding-energy spectra in the region of plasmon satellites.

To simulate the finite experimental energy resolution $\delta\varepsilon$ we substitute the δ function in the definition of the SMD (12) by a normalized Gaussian $G[(\varepsilon-E_{j\mathbf{k}})/\delta\varepsilon)]$. We exploit the fact that the energy of the ejected electron in the bulk is fixed and add the corresponding Gaussian function to the left-hand side of Eq. (15). We combine it with the squared momentum space coefficient to produce the SMD of the unoccupied final states:

$$I(\varepsilon)\propto f_{ee}\int_{\Delta\Omega_2} d\Omega_2 \sum_{\mathbf{g}} \rho(\mathbf{p}_{2\parallel}-\mathbf{g},q_{2\perp};E_2+\Phi)\rho(\mathbf{q},\varepsilon) \times \delta_{\mathbf{q}+\mathbf{Q},\mathbf{q}_2}. \tag{16}$$

We notice that the polar angle integration has a different effect on the SMD of the initial and final target states in Eq. (16). The SMD of the final states varies slightly as we rotate $\mathbf{p}_{2\parallel}$. This is so because of a relatively small anisotropy of energy bands and momentum densities of graphite in the basal plane (see, for instance, Fig. 2). In contrast, the SMD of the initial state $\rho(\mathbf{q},\varepsilon)$ changes significantly since the rotation in the surface plane changes alignment of the vectors $\mathbf{q}_2$ and $\mathbf{Q}$, the latter being bound to the scattering plane. Therefore we can take the spherically averaged SMD of the final states out of the integral and present Eq. (16) in the form

$$I(\varepsilon)\propto f_{ee}\sum_{\mathbf{g}} \rho(p_{2\parallel}-g,q_{2\perp};E_2+\Phi) \times \int_{q_\parallel^{\min}}^{q_\parallel^{\max}} dq_\parallel \int_{q_\perp^{\min}}^{q_\perp^{\max}} dq_\perp \int_0^{\pi/6} d\varphi_q \rho(\mathbf{q},\varepsilon)\,\delta_{\mathbf{q}+\mathbf{Q},\mathbf{q}_2}. \tag{17}$$

Here the polar angle integration simulates the rotational disorder of HOPG, which is only aligned in the direction along the rotational axis $\hat{\mathbf{c}}$.

The integration boundaries in Eq. (17) calculated at $\mathbf{g}=0$ are given in Table I. The range of $q_\perp$ is very small for the grazing-angle geometry. Projection of the integration region on the basal plane is contained within the first BZ except for the ejection energy of 14.2 eV for which it slightly overlaps with the second BZ in the ΓM direction. The size of the first BZ of graphite is 0.78 and 0.90 a.u. in the ΓM and ΓK directions, respectively.

Reciprocal vector translation moves the integration area in Eq. (17) beyond the first BZ. In practice we found it sufficient to include only two shortest $\mathbf{g}$ vectors,

$$\mathbf{g}_1=(1,1/\sqrt{3})\times 2\pi/a,$$
$$\mathbf{g}_2=(0,2/\sqrt{3})\times 2\pi/a, \tag{18}$$

where $a=4.65$ a.u. is the lattice parameter of graphite. These vectors translate the integration area into the second and third BZ's as shown in Fig. 3. We found that further translations with larger reciprocal vectors have little contribution to the sum in Eq. (17) since the SMD is very small in this region.

To calculate numerical values of the SMD in Eq. (17) we employed the linear muffin-tin orbital (LMTO) method in the atomic sphere approximation, as described by Skriver.[15] We used the von Barth–Hedin parameterization for the exchange-correlation potential.[16] Momentum density calculation on graphite within the LMTO formalism was described in Ref. 17. As compared to this earlier work we employ here a larger set of the fictitious empty muffin-tin spheres (eight instead of two) to have a better representation of the electron potential inside a loosely packed graphite unit cell. The momentum space coefficients of the unoccupied electron states are also obtained from the same LMTO calculation. However, presently we use the single set of the energy-independent LMTO orbitals optimized to give the best representation of the valence band. To get an accurate description of the conduction band this set should be at least doubled as was demonstrated by Ahuja *et al.*[18] So the accuracy of our description of the conduction band is diminishing as the energy of the final electron state increases.

Convenient graphical analysis of Eq. (17) can be performed by using the plot of Fig. 6 in which the SMD $\rho(\mathbf{q},\varepsilon)$ is plotted versus $q_\parallel$ (horizontal scale) and ε (vertical scale) at a given $q_\perp$. The value of the momentum density is indicated by various shades of gray, the darker areas representing larger density. The plot of Fig. 6 corresponds to the smallest ejection energy $E_2=3.7$ eV. Usually $\rho(\mathbf{q},\varepsilon)$ is defined for the occupied states only. Here we extend it above the Fermi level and include the unoccupied states as well. For the grazing-angle geometry $Q_\perp$ is negligible and therefore $q_{2\perp}\simeq q_\perp$. So we can use the same plot to visualize the SMD of both the occupied and empty states in Eq. (17).

In Fig. 6 we see the occupied σ and π bands, which constitute the valence band of graphite. We note that the three σ bands indicated as separate bands in Fig. 2 join each other smoothly and form a single parabola in the extended momentum space. The π band continues above the Fermi level. Here also starts the unoccupied σ^* band which is formed from the empty $3s$ orbital of the carbon atom.

The ejected electron state in the solid is represented in Fig. 6 by the points with the abscissa $|p_{2\parallel}-g|$ and the ordinate $E_2+\Phi$. These points at $\mathbf{g}=0$ are indicated by the intersection of straight lines in Fig. 6. Another set of points which corresponds to the $\mathbf{g}$ vectors of Eq. (18) is shifted outwards along the horizontal line by 0.78 a.u. We see from the plot

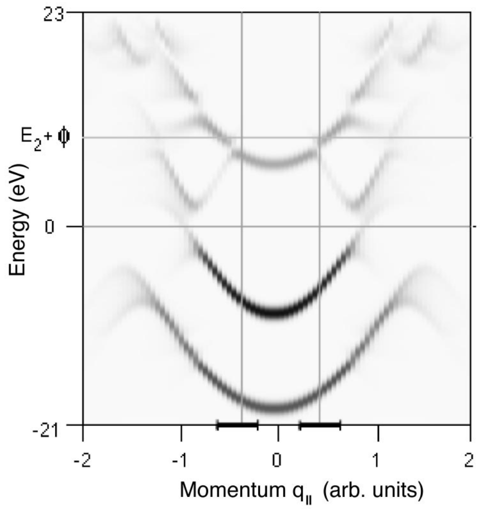

FIG. 6. The spectral momentum density of HOPG extended to the unoccupied states. Ejected electron energy $E_2=3.7$ eV and $q_\perp = 0.67$ a.u. Straight lines indicate the final state of the ionnized electron. Highlighted is the area of the valence electron momentum, which gives rise to the direct escape of the ionized electron into the vacuum (See Table I). On the right are the binding-energy spectra corresponding to the direct and **g**-assisted escape of the ionized electron as well as the total spectrum.

that the momentum density is approximately equal for the direct ($\mathbf{g}=0$) and **g**-assisted escape of the ejected electron into the vacuum.

The δ-function $\delta_{\mathbf{q}+\mathbf{Q},\mathbf{q}_2}$ projects the fixed $q_{2\|}$ final state into the finite $q_{\|}$-size initial state because of the variable angle between $\mathbf{q}_2$ and $\mathbf{Q}$. The range of $q_{\|}$ for the direct escape is highlighted on the x axis in the SMD plot of Fig. 6. The transition that leads to the direct escape originates in the first BZ where only σ_1 and π bands have siginificant presence (see Fig. 2). Integrated over the range of $q_{\|}$ these bands give two well-separated peaks in the binding-energy spectrum as indicated on the right side of Fig. 6. The region of the initial-state momentum that gives rise to the **g**-assisted escape is populated by the σ_2 and σ_3 bands and gives rise to the peak in the binding-energy spectrum in between the σ_1 and π. When added up with an equal weighting factor the direct and **g**-assisted binding-energy spectra span nearly continuously the whole valence band.

The similar SMD plots can be produced for the higher ejected electron energies $E_2=8.0$ and 14.2 eV. With these energies, however, we encounter considerable difficulty trying to represent the final state of the ejected electron in the bulk. Both the directly escaped electron and that assisted with the **g** vectors fall into the region of a very small momentum density of the final states. This can be interpreted in the following way. In derivation of our formalism we assume that the perpendicular component of the ejected electron $q_\perp$ is determined through the energy conservation (6). The band energies of graphite $E_{j\mathbf{k}}$, at least in the valence region, depend very weakly on $k_\perp$. The first unoccupied σ^* band shows a small dispersion of about 2 eV with respect to $k_\perp$.[19] This, however, might not be sufficient to match an arbitrary combination of $\mathbf{p}_2$ and E_2 in the vacuum, which is determined solely by the experimental kinematics. If matching is not possible through the bulk states it occurs only through the surface states. This is accompanied by a significant reduction in the ejected electron current even in the noncoincident mode. This effect was detected experimentally. As the energy of the ejected electron increases it falls into the region of the higher unoccupied bands, which acquire gradually the

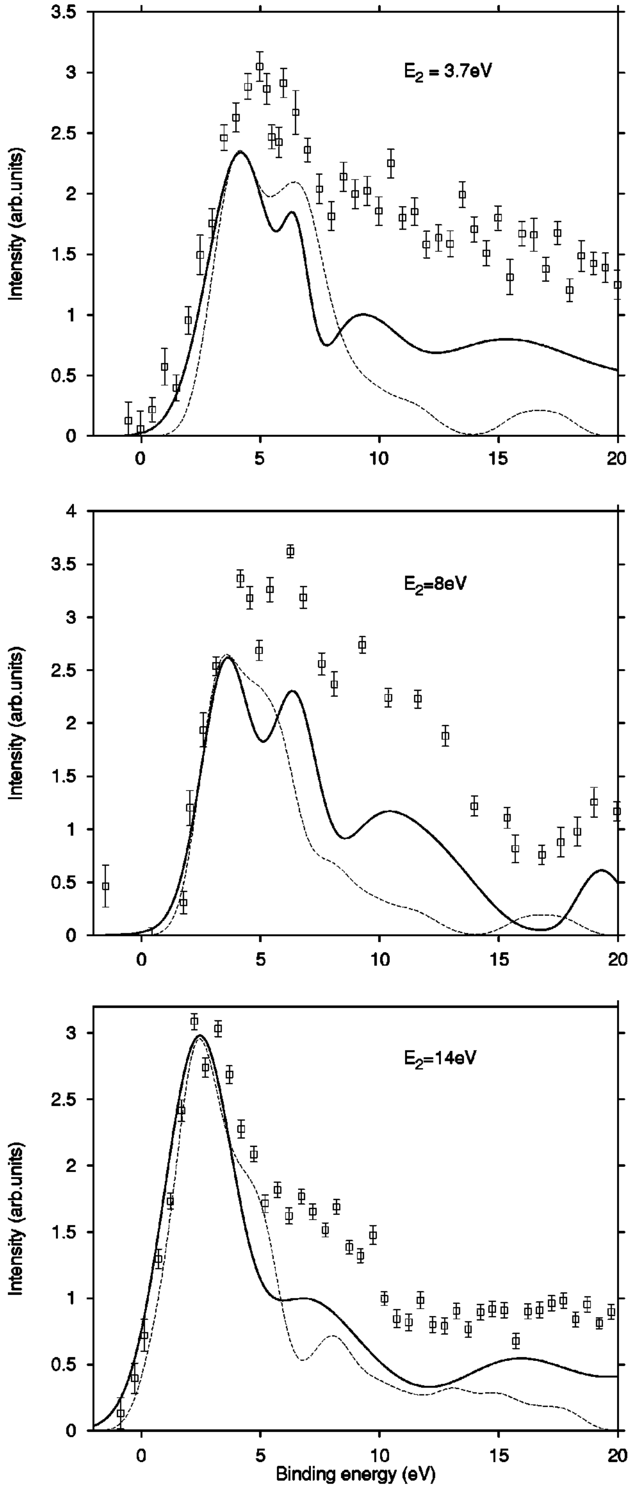

FIG. 7. Measured and calculated (e,2e) intensity at various ejection energies. The experiment (error bars) is deconvoluted with respect to the multiple scattering of the fast incident electron and shown as the solid line. The calculated spectrum is shown as the dashed line.

3D character and a free-electron-like dispersion. Then the matching becomes possible for any values of $\mathbf{p}_2$ and E_2, which is the situation of the high-energy $(e,2e)$.

In order to overcome this difficulty and proceed any further we simply assume that the intensity of the direct and **g**-assisted processes are the same. This might not be a well-justified assumption. Nevertheless it allows us to make important observations about the mechanism of the present $(e,2e)$ reaction.

The final results of our computations are shown in Fig. 7 for ejected electron energies $E_2 = 3.7$, 8, and 14.2 eV. As compared with the binding-energy spectra shown on the right side of Fig. 6 they also include the dynamical factor $f_{ee} \propto Q^{-4}$, which decreases rapidly from the top to the bottom of the valence band. The experiment is normalized to the maximum calculated intensity. Since the binding energy is measured relative to the vacuum level but calculated with respect to the Fermi level, the experimental curve is shifted horizontally by the amount of $E_F = 5.5$ eV. This value was found by an independent measurement.

The experimentally observed $(e,2e)$ intensity was deconvoluted with respect to the energy losses of the fast incident electron. No similar deconvolution was made for the slow ejected electron since its mean free path is of the order of a magnitude larger. The deconvoluted $(e,2e)$ intensity was fitted with four Gaussian peaks of equal width corresponding to the experimental energy resolution of 1.2 eV and representing three σ and π bands of graphite.

The agreement between the calculation and measurement is rather satisfactory, especially if we recall that we use a very crude approximation by assuming *ad hoc* the equal intensities of the direct and **g**-assisted escape of the ejected electron into the vacuum. There might be also additional factors that worsen agreement between the measured and calculated spectra. In the experimental spectra there is a large background intensity at energies well below the bottom of the valence band ($\epsilon > 20$ eV). This might be due to the intrinsic loss events associated with collective response of the valence electrons and not describable within the independent particle approximation. These processes are related to the dielectric function appearing in Eq. (13) but not properly evaluated in the present study.

IV. CONCLUSION

We develop the momentum space wave function formalism to describe the process of a slow electron ejection from a crystal by electron impact at a high or moderate incident energy. The amplitude of the slow electron ejection is presented as a product of the momentum space wave functions of the target electron in the initial state in the valence band, and the final state in the conduction band. Because of the selective population of the target electron momentum space the largest contribution to the transition amplitude comes from the transition between the states with a well-defined *real* momentum corresponding to a particular section of the BZ. In the limit of the large energy transfer the transition amplitude contains only the target electron momentum space wave function in the valence band.

The bulk transition that leads to the electron escape into the vacuum can be depicted graphically on the plot of the SMD $\rho(\mathbf{q},\varepsilon)$ displayed as a function of $q_\parallel$ and ε at the fixed $q_\perp$. The initial state of the transition is represented by the SMD of the valence band in the finite interval of $q_\parallel$. The final state of the ionized electron in the bulk is restricted to the several points on the SMD diagram that correspond to the direct ($\mathbf{g}=0$) and **g**-assisted escape of the ionized electron into the vacuum. This final state should be matched in ε and $q_\parallel$ by the plane wave in the vacuum. This is achieved by adjusting $q_\perp$ which is not bound by the law of momentum conservation because of the termination of the surface of the crystal. In the case of graphite, because of its layered quasi-2D structure, this matching is not always possible and the final ionized state falls into the region of a very small SMD. This causes a strong reduction of the ejected electron current even in a noncoincident mode.

The processes of the direct and **g**-assisted escape of the ionized electron into the vacuum take their origin in different and nonoverlapping areas of the valence electron momentum space. The direct process can only start from the two occupied bands, σ_1 and π, whereas the **g**-assisted process involves the σ_2 and σ_3 bands. We were able to make this conclusion because the dynamics of the present $(e,2e)$ reaction is reduced to just a single mechanism of the reflection followed by the inelastic scattering. This mechanism is dominant since it allows for the smallest amount of the momentum transfer and therefore the largest Mott cross section. Although the kinematics of the slow ejected electron is not fully determined in the present experiment, the boundaries of the target electron momentum were narrow enough to exclude the contribution from the second and third BZ in the direct process.

The complete theoretical description of the low ejection energy $(e,2e)$ experiments on the surface of graphite requires an accurate band-structure calculation in the conduction band. This, in principle, is possible within the LMTO method but requires a substantial enlargement of the basis set of energy-independent orbitals. Experimentally, it would be more advantageous to resolve fully the ejected electron momentum and perform an $(e,2e)$ reaction on the surface of crystalline rather than rotationally disordered graphite. These developments in theory and experiment are currently underway and make us hopeful to achieve a better understanding of the physics of the electron-impact ionization of solids.

ACKNOWLEDGMENTS

The authors are very thankful to M. Vos and J. Berakdar for useful and constructive discussions. We gratefully acknowledge J. Kirschner, R. Feder, and O. Samarin for their critical reading of the manuscript. One of the authors (A.S.K.) wishes to thank the staff of the Physics Department of the Università di Roma Tre for their hospitality and much needed help. This work was partially supported by Progetto Coordinato del Comitato Fisica CNR.

---

[*] Permanent address: Institute of Advanced Sciences, Research School of Physical Sciences and Engineering, Australian National University, Canberra ACT 0200, Australia.

[1] M. Vos and I. E. McCarthy, Rev. Mod. Phys. **67**, 713 (1995).

[2] J. R. Dennison and A. L. Ritter, J. Electron Spectrosc. Relat. Phenom. **77**, 99 (1996).

[3] J. Kirschner, O. M. Artamonov, and S. N. Samarin, Phys. Rev. Lett. **75**, 2424 (1995).

[4] H. Gollisch, D. Meinert, X. Yi, and R. Feder, Solid State Commun. **102**, 317 (1997).

[5] S. Iacobucci *et al.*, J. Electron Spectrosc. Relat. Phenom. **67**, 479 (1995).

[6] S. Iacobucci *et al.*, Phys. Rev. B **51**, 10 252 (1995).

[7] S. Rioual *et al.*, Phys. Rev. B **57**, XX (1998).

[8] S. Hüfner, *Photoelectron Spectroscopy*, edited by M. Cardona, P. Fulde, K. von Klitzing, and H.-J. Queisser, Vol. 82 of *Springer Series in Solid-State Science* (Springer-Verlag, Berlin, 1995).

[9] J. Berakdar and M. P. Das, Phys. Rev. A **56**, 1403 (1997).

[10] O. M. Artamonov, S. N. Samarin, and J. Kirschner, Appl. Phys. A: Mater. Sci. Process. **65**, 535 (1997).

[11] J. C. Slater, *Quantum Theory of Molecules and Solids* (McGraw-Hill, New York, 1965).

[12] P. Goodman and A. F. Moodie, Acta Crystallogr., Sect. A: Cryst. Phys., Diffr., Theor. Gen. Crystallogr. **30**, 280 (1974).

[13] L. D. Landau, *Quantum Mechanics: Non-Relativistic Theory*, Vol. 3 of *Course of Theoretical Physics* (Pergamon Press, New York, 1977).

[14] C. Kittel, *Introduction to Solid State Physics* (Wiley, New York, 1986).

[15] H. L. Skriver, in *The LMTO Method*, edited by M. Cardona, P. Fulde, and H.-J. Queisser, Springer Series in Solid-State Science, Vol. 41 (Springer-Verlag, Berlin, 1984).

[16] U. von Barth and L. Hedin, J. Phys.: Condens. Matter **5**, 1629 (1972).

[17] A. S. Kheifets and M. Vos, J. Phys.: Condens. Matter **7**, 3895 (1995).

[18] R. Ahuja *et al.*, Phys. Rev. B **55**, 4999 (1997).

[19] Th. Fauster, F. J. Himpsel, J. E. Fischer, and E. W. Plummer, Phys. Rev. Lett. **51**, 430 (1983).